Generation, amplification, frequency conversion and reversal of propagation of THz photons in nonlinear hyperbolic metamaterial

ALEXANDER K. POPOV[1,*] AND SERGEY A. MYSLIVETS[2,3]

[1] Birck Nanotechnology Center, Purdue University, West Lafayette, IN 47907, USA
[2] Kirensky Institute of Physics, Federal Research Center KSC SB RAS, 50, Akademgorodok, Krasnoyarsk 660036, Russia,
[3] Siberian Federal University, 79 Svobodny Av., Krasnoyarsk, 660041, Russia
[*] Corresponding author: popov@purdue.edu

Extraordinary properties of three-wave mixing and greatly enhanced optical parametric amplification are numerically investigated in the proposed hyperbolic metamaterial made of carbon nanotubes. It supports a set of normal and backward electromagnetic modes with equal co-directed phase velocities and contra-directed energy fluxes in the THz frequency range.

Backward electromagnetic waves (BEMWs) are the extraordinary waves with contra-directed phase velocity and energy flux. They do not exist in the naturally occurring materials. However, with the advent of nanotechnology, it became possible to deliberately engineer the nanostructures which produce such a significant delay of the electromagnetic response that it effectively gives rise to BEMWs [1]. Optical BEMWs enable numerous breakthroughs in photonics, such as super-resolution and cloaking. Besides applications in the linear optics, extraordinary coherent, i.e. phase dependent, nonlinear optical (NLO) propagation processes have been predicted which hold the promise of significant advances in the harvesting of light. Among them are the processes of generation, amplification, modulation, frequency-conversion, and the propagation direction reversal of the light waves [2–4]. A main approach to produce the optical BEMWs is grounded on the engineering of the metamaterials (MMs) with negative refractive index [1]. In this work, we employ an approach to the outlined advancements which is based on the guided EMW with variable positive to *negative* spatial dispersion [5]. In the case of negative spatial dispersion $\partial \omega / \partial k < 0$, the Poynting vector $\mathbf{S} = \mathbf{v}_g U$ (U is the energy density), which is directed along the group velocity $\mathbf{v}_g = (\mathbf{k}/k)(\partial \omega / \partial k)$, and the phase velocity, which is directed along the wave vector $\mathbf{k}$, appear contra-directed. The negative spatial dispersion can be realized in hyperbolic MMs [6]. However, the key point of our work is as follows. As shown in [2], a huge enhancement in the coherent NLO coupling, such as in three-wave mixing, and in the related optical parametric am-
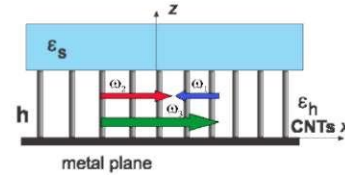

Fig. 1. Metamaterial composed of standing CNTs.

plification (OPA) and frequency conversion occurs only if the energy fluxes of the coupled waves are *contra-directed*, whereas their phase velocities are *co-directed* and *equal*. This imposes a set of strict requirements to the MMs being engineered. In this paper, we propose a model of such a MM which can operate in the THz and near-IR frequency ranges. Extraordinary NLO processes which give rise to the OPA and to the frequency and propagation direction changes are investigated and the outcomes are demonstrated through numerical simulations. The applications may include ultra-miniature amplifiers, frequency changing reflectors and remotely actuated sensors in the THz. The reported approach can be extended on other constituent materials and frequency ranges.

Consider a MM slab made of carbon nanotubes (CNTs) of height h standing on the perfectly conducting metal surface and embedded in the host dielectric with the relative permittivity ϵ_h. On the top, it is bounded by the dielectric with the relative permittivity ϵ_s (Fig. 1). The CNTs form a two-dimensional periodic

structure in the xy-plane with a square lattice constant d. Basically, a shape of the lattice can be modified. Carbon nanotubes possess strongly anisotropic metallic property along the axis z which determines the negative relative permittivity c_{zz} [7–9]

$$c_{zz} = 1 - k_p^2/(k^2 + i\xi k), \; k_p^2 = \mu_0/(d^2 L_0). \quad (1)$$

Here, $k = \omega/c < k_p$, k_p is the effective plasma wavenumber, L_0 is the effective inductance of the CNTs per unit length, the parameter $\xi = 1/c\tau$ is responsible for losses, τ is the electron relaxation time. Radius r of the CNTs and the lattice constant d are taken to be $r = 0.82$ nm and $d = 15$ nm. Then the indicated parameters are estimated as $L_0 = 3.7 \times 10^{-3}$ H/m, $k_p^2 = 1.51 \times 10^{12}$ m^{-2}, $\omega_p/2\pi = 58.7$ THz, $\tau = 3$ ps [8, 9]. Thus the MM can be thought of as the medium with hyperbolic dispersion for the frequencies below ω_p, because then $c_{zz} < 0$, whereas $c_\perp = c_{xx} = c_{yy} = c_h > 0$. As shown below, the fact that the CNTs have a limited height plays a crucial role in achieving the stated goal. The MM depicted in Fig. 1 can be also thought of as a *tampered waveguide* formed by the metal plate and by the upper dielectric layer. Space-time dependence of the fields propagating along the waveguide can be approximated as $\exp[i(k_x x - \omega t)]$. Maxwell equations for the allowed modes split into two sub-systems: for the TM-modes with $H_x = 0$, $H_z = 0$, $E_y = 0$, and the TE-modes with $E_x = 0$, $E_z = 0$, $H_y = 0$. Equations for the tangent components of the TM and TE modes respectively are:

$$dE_x(z)/dz = i\eta \left[k - (k_x^2/kc_{zz}) \right] H_y,$$
$$dH_y(z)/dz = i(k/\eta) E_z = -(k_x/kc_{zz})\eta H_y. \quad (2)$$

$$dE_y(z)/dz = -i\eta k H_x, \; H_z = (k_x/k\eta) E_y,$$
$$dH_x(z)/dz = (i/\eta) \left[(k_x^2/k) - kc_\perp \right] E_y. \quad (3)$$

Here, $\mu = 1, \eta = (\mu_0/c_0)^{1/2}$. Since $c_{zz} < 0$ and $c_\perp > 0$, only TM-modes exhibit the hyperbolic dispersion and are of interest.

The system (2) can be presented in a matrix form:

$$dX(z)/dz = i[A]X(z) \quad (4)$$

with the column-vector $X = (E_x, H_y)_{col}$ and elements of the matrix [A] defined by Eq. (2). The solution to the Cauchy problem for this matrix equation is

$$X(z) = \exp\{i[A]z\}X(0). \quad (5)$$

Here, $[M](z) = \exp\{i[A]z\}$ is the transfer matrix or the propagator which connects the tangent field components in planes $z = 0$ and z. The propagator can be computed using spectral representation of the matrix function. In our case, the matrix exponent is expressed as [10]:

$$\exp\{i[A]z\} = \sum_{l=1}^{s} \exp\{i\lambda_l z\} \prod_{k \neq l} \frac{[A] - \lambda_k[I]}{\lambda_l - \lambda_k}, \quad (6)$$

where s is the number of different eigenvalues λ_k of the matrix [A], and [I] is the unit matrix. In our case, $s = 2$ and

$$\lambda_{1,2}^2 = k_z^2 = c_\perp \left[k^2 - (k_x^2/c_{zz}) \right]. \quad (7)$$

Using Eq. (6) one obtains an expression for matrix [M]:

$$M_{11}(z) = \cos(k_z z), \; M_{12}(z) = iZ\sin(k_z z),$$
$$M_{21}(z) = i\sin(k_z z)/Z, \; M_{22}(z) = \cos(k_z z), \quad (8)$$

where $Z = E_x/H_y = \eta k_z/kc_\perp$ is the transverse wave impedance for the TM-waves. The tangent field components can be recalculated from the ground plane $z = 0$ to the upper plane $z = h$ using the transfer matrix while taking into account the perfect electrical conducting conditions at $z = 0$:

$$E_x(h) = M_{12}H_y(0), \; H_y(h) = M_{22}H_y(0). \quad (9)$$

Since the area at $z > h$ is a semi-infinite material with the relative permittivity c_s, the tangent electric and magnetic field components at $z = h$ are connected via the transverse impedance

$$Z_s = E_x(h)/H_y(h) = \eta k_z/kc_s = i\left[\eta \sqrt{k_x^2 - k^2 c_s} \right]/kc_s. \quad (10)$$

Here, Eq. (7) is used and the waves are supposed to be exponentially decaying from the surface of the MM, i.e. $k_x^2 > k^2 c_s$. With aid of Eqs. (8) - (10), one obtains a dispersion equation for the TM-modes propagating along the x-axis [12]:

$$k_z \tan(k_z h) = (c_h/c_s)\sqrt{k_x^2 - k^2 c_s}, \quad (11)$$

where $k_z = \sqrt{c_h[k^2 - (k_x^2/c_{zz})]}$, $k_x^2 > k^2$. Dispersion Eq. (11) reminds the one predicted in [13] for a layered MM. It is seen that the open-end structure imposes a significant difference on the waves dispersion as compared with an unbounded uniaxial crystal [11]:

$$k_x^2 = c_{zz}(k^2 - k_z^2). \quad (12)$$

It also contrasts with the case of the MM made of CNTs standing between two perfectly conducting planes:

$$k_x^2 = c_{zz}\left[k^2 - (m\pi/2h)^2 \right]. \quad (13)$$

Here, $k_z = m\pi/2h$, h is the height of the waveguide, and m is a positive integer determining the number of field variations along the CNTs. It is seen that all allowed discrete EM modes corresponding to different values of m at $c_{zz} < 0$ and $k < m\pi/2h$ appear BEMWs, since $dk_x^2/dk^2 < 0$. On the contrary, Eq. (11) predicts the mode with a sign-changing dispersion which is of a paramount importance for enabling the coexistence of the ordinary and BEMWs. Note, the dispersion given by Eq. (11) is *strongly dependent* on the CNTs height h.

A spectrum of the allowed modes and their attenuation can be found by numerically solving Eq. (11) and calculating the complex propagation constant $k_x = k_x' + ik_x''$. Figure 2(a) presents a spectrum of the lowest modes and their dispersion $\omega(k_x')$ calculated for $h = 3.5 \; \mu$m. For the sake of simplicity, we assume further that $c_h = c_s = 1$. Reduced wavevector $k_x'/k = c/v_{ph}$ represents phase velocity v_{ph}. It proves the possibility of the phase-matching for the three-wave mixing frequency down conversion process $\omega_3 - \omega_2 = \omega_1$ and OPA at ω_2. The simulations also prove the possibility of the phase matching for *different* sets of frequencies by adjusting the nanotube lengths h. For convenience, a sum of the mode frequencies $\omega_1 + \omega_2$ is shown by the dashed line. However, only its crossing with the third mode satisfies frequency mixing. Phase matching occurs at $k_x'/k = 1.447$ (marked with the vertical line). Figure 2(b) depicts attenuation of the respective modes. As seen, the attenuations may differ greatly despite the fact that electron relaxation rate is the same. The difference is due to the nanowaveguide propagation regime. Figure 3 depicts group velocity indices for the respective modes. Split for the second mode indicates slow-light regime $v_{gr} \to 0$. It is seen that in

Table 1

Mode	f, THz	k, 10^5 m^{-1}	$|k_x''/k|$, 10^{-3}	n_g	$\alpha = 2k_x''$, $10^{-2}\,\mu$m^{-1}	L_a, μm	λ_{vac}, μm	λ_{med}, μm
1	10.43	2.186	2.26	1.45	0.988	2331	28.74	19.86
2	34.95	7.325	17.8	−7.71	2.61	88.2	8.58	5.93
3	45.38	9.511	15.46	−6.29	2.94	78.3	6.61	4.57

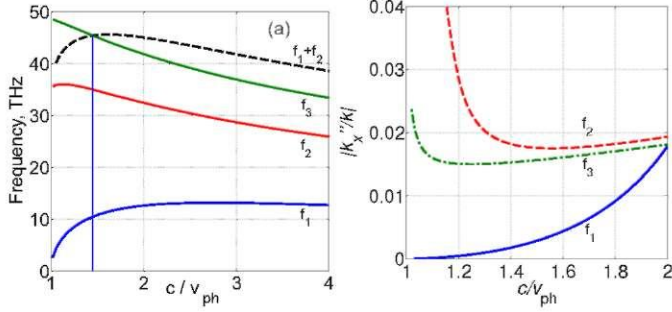**Fig. 2.** (a) Dispersion of three lowest modes at $h = 3.5\,\mu$m. The dashed line represents the sum of two lowest modes. (b) Normalized attenuation constant k_x''/k: the blue (solid) line corresponds to f_1, the red one (dashed) – to f_2, the green one (dash-dotted) – to f_3.
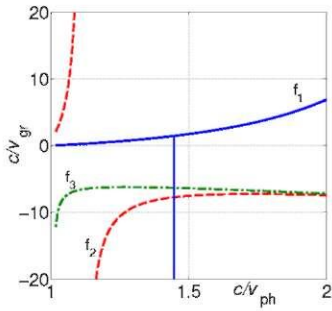

Fig. 3. Group velocity indices c/v_{gr} for the respective modes.

the vicinity of phase matching group velocities at f_2 and f_3 are directed *against* the phase velocity with the values significantly less than the speed of light. Alternatively, group velocity for the first mode is of the opposite sign.

At the pump pulse duration $\Delta\tau = 10$ ps, the pulse spectrum bandwidth is $\Delta f \approx 1/\Delta\tau = 0.1$ THz, i.e., $\Delta f / f \propto 10^{-2} \div 10^{-3}$. Hence, the pump can be treated as quasi-monochromatic. Alternatively, for $\Delta\tau = 10$ fs, $\Delta f / f \propto 10$, the spectrum covers all modes. The data used for the simulations described below is summarized in Table 1. The values L_a indicate the metaslab length corresponding to attenuation $I_i/I_{i0} = \exp(-\alpha_i L_{ai}) = 0.1$, i.e., $\alpha_i L_{ai} = 2.3$ for the respective frequencies. A thickness $L = L_{a3} = 78.3\,\mu$m was chosen to satisfy $\alpha_3 L_{a3} \approx 2.3$ for the mode with highest attenuation. For the same slab thickness, $\alpha_{a2}L = 2.04$, and $\alpha_{a1}L = 0.077$. Therefore, attenuation at the lowest frequency appears significantly less than for the two others which are comparable. Pump pulse length for $\Delta\tau = 10$ ps is $l = \Delta\tau v_{3gr} = \Delta\tau(c/n_{3gr}) = 477\,\mu$m, i.e., about 6 times greater than L_{a3}. Hence, in this case, a quasi-stationary process establishes through the major part of the pulse. Transient processes at the forefront and at the tail of the pulse can be neglected.

Normalized amplitudes of the waves are given by the following equations which account for the fact that propagation direction of the wave at f_1 must be opposite to others in order to satisfy the phase matching:

$$(\partial a_1/\partial\xi) - (v_3/v_1)(\partial a_1/\partial\tau) = -igla_3 a_2^* + (\tilde{\alpha}_1/2d)a_1, \tag{14}$$

$$(\partial a_2/\partial\xi) + (v_3/v_2)(\partial a_2/\partial\tau) = igla_3 a_1^* - (\tilde{\alpha}_2/2d)a_2, \tag{15}$$

$$(\partial a_3/\partial\xi) + (\partial a_3/\partial\tau) = ig^* la_1 a_2 - (\tilde{\alpha}_3/2d)a_3. \tag{16}$$

Here, $\xi = x/l$, $l = v_3\Delta\tau$, $\tau = t/\Delta\tau$, $d = L/l$, $\tilde{\alpha}_i = a_j L$, $v_i > 0$ and α_i are the modules of group velocities and attenuation indices at the corresponding frequencies, $g = \text{æ}E_{30}$, $E_{i0} = E_i(x = 0)$, $\text{æ} = 4\pi\sqrt{k_1 k_2}\chi_{\text{eff}}^{(2)}$, $\chi_{\text{eff}}^{(2)}$ is effective nonlinear susceptibility, $a_i = \sqrt{|c_i c_3|/k_i k_3}(E_i/E_{30})$. Quantities $|a_i|^2$ are proportional to the time dependent photon fluxes. The input pulse shape at f_3 was chosen to be close to a rectangular form

$$F(\tau) = 0.5\left(\tanh\frac{\tau_0 + 1 - \tau}{\delta\tau} - \tanh\frac{\tau_0 - \tau}{\delta\tau}\right), \tag{17}$$

where $\tau = t/\Delta\tau$, $\delta\tau$ is the duration of the pulse front and tail, and τ_0 is the shift of the front relative to $t = 0$. The values $\delta\tau = 0.01$ and $\tau_0 = 0.5$ were taken for the simulations. The input signal at f_2 was supposed to be a continuous wave with $a_{20} = 10^{-5}a_{30}$.
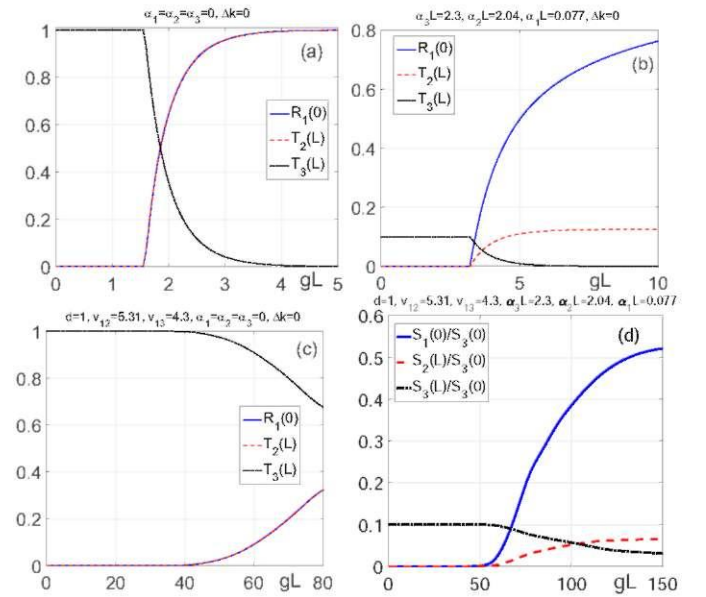

Fig. 4. Optical parametric amplification and frequency-shifting NLO reflectivity vs. intensity of the pump.

Figure 4 demonstrates the dependence of the output amplified signal at f_2 and of the idler at f_1 generated in the opposite direction on the intensity of the pump as well as the ef-
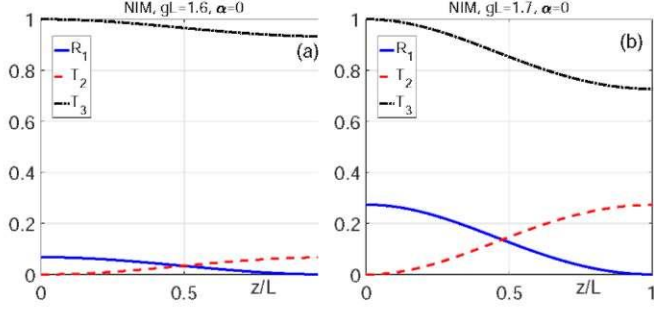
Fig. 5. Fields distribution along the attenuation-free metaslab in the vicinity of the resonance pump intensity.
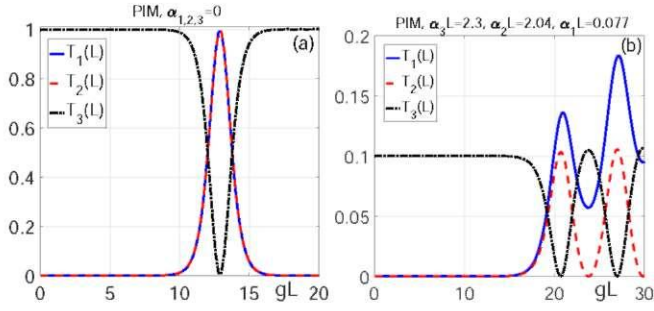

Fig. 6. Output fields vs intensity of the pump for the ordinary, co-propagating coupling scheme. All other parameters are the same as in Figs. 4 (a) and (b) respectively.

fects of attenuation and the pump pulse duration on the outputs. Panels (a) and (b) depict the cases of a long pump pulse (quasi-CW regime). Here, $T_{2,3}(x = L) = |a_{2,3}(L)/a_{30}|^2$ are the transmission factors, and a_{30} is the input pump maximum. The value $T_2(L)$ represents OPA. Nonlinear optical reflectivity (NLOR) at f_1 is given by the value $R_{10} = |a_1(x = 0)/a_{30}|^2$. Panel (a), which corresponds to the attenuation-free regime, shows that a huge enhancement in the OPA and in the NLOR occurs when the pump intensity reaches a certain threshold value. This is the effect specific to BW coupling which originates from the appearance of the intensity-resonant distributed NLO coupling feedback [2]. Here, photon conversion efficiency reaches 100% at a relatively small increase of the pump above the threshold value. Attenuation significantly decreases OPA (panel (b)). Remarkably, NLOR does *not* experience such a significant decrease. It is because the reflected wave is predominantly generated near the MM entrance where the pump and the signal are not yet significantly attenuated. Besides that, the attenuation for the f_1 mode appears to be significantly less than the one for the two other modes. Panels (c) and (d) depict the case of a shorter pulse $l = L$. Here, the transmitted and reflected photon fluxes per pulse are given by the values $S_i(x)/S_{30} = \int dt |a_i(x,t)|^2 / \int dt |a_{30}(t)|^2$. It is seen that the dispersion and the opposite signs of group velocities cause a significant increase of the pump threshold and a decrease of the sharpness of the enhancement in the vicinity of the threshold.

The described dependencies are due to the unusual Manley-Rowe relationship. A *difference* of the pump and of the *contra-propagating* idler photon numbers is a constant along the slab, whereas the *sum* of the pump and of the *co-propagating* signal photon numbers is a constant as seen in Fig. 5 calculated for the

ultimate case of the attenuation-free metaslab. A width of the gap between the pump and the idler curves represents a conversion rate. The gap sharply decreases and the conversion rate increases in the vicinity of the threshold pump intensity.

Figure 6 is calculated for the co-propagating coupling in an ordinary material with the same other parameters as in Figs. 4 (a) and (b). It is seen that higher conversion efficiency at lower pump intensity is achieved in the first BEMW coupling case.

CONCLUSIONS: The possibility of engineering the metamaterials which enable a great enhancement of coherent nonlinear optical coupling of electromagnetic waves is shown. This allows for the decreasing of the size of a material slab which is needed for the efficient frequency conversion and optical parametric amplification of signals. The proposed metamaterials support a set of the guided electromagnetic modes whose dispersion $\omega(k)$ can be adjusted so that their frequencies would satisfy the wave mixing while their propagation phase velocities become equal. The latter is the prerequisite of a fundamental importance for efficient nonlinear optical frequency mixing. The even more important point is that the proposed metamaterials enable the modes with oppositely directed energy fluxes while their phase velocities are co-directed and equal. Indeed, the latter is a key factor that ensures a great enhancement in the wave coupling. Besides the enhanced parametric amplification of weak signals and compensating their losses, such an uncommon coupling scheme enables generation of the extraordinary frequency shifted idler in the direction opposite to the signal. Such possibility is demonstrated through numerical simulations of the corresponding propagation processes with the aid of a particular model of the metamaterial suitable for the THz frequency range. The outlined properties of the investigated processes hold promise for applications in the photonic device technologies and in the remote sensing.

We thank I. S. Nefedov for helpful discussions.

REFERENCES

1. W. Cai and V. Shalaev, *Optical metamaterials, fundamentals and applications* (Springer-Verlag, New York, 2010), 1st ed.
2. A. K. Popov and V. M. Shalaev, Appl. Phys. B: Lasers and Optics **84**, 131 (2006).
3. I. V. Shadrivov, A. A. Zharov, and Y. S. Kivshar, J. Opt. Soc. Am. B **23**, 529 (2006).
4. M. Lapine, I. V. Shadrivov, and Y. S. Kivshar, Review of Modern Physics **86**, 1093 (2014).
5. A. K. Popov, M. I. Shalaev, S. A. Myslivets, V. V. Slabko, and I. S. Nefedov, Appl. Phys. A **109**, 835 (2012).
6. A. Poddubny, I. Iorsh, P. Belov, and Yu. Kivshar, Nat. Phot. **7**, 948 (2013).
7. I. V. Lindell, S. A. Tretyakov, K. I. Nikoskinen, and S. Ilvonen, Microwave and Optical Technology Letters **31**, 129 (2001).
8. I. Nefedov and S. Tretyakov, Photonics and Nanostructures – Fundamentals and Applications **9**, 374 (2011).
9. I. Nefedov and S. Tretyakov, Phys. Rev. B **84**, 113410 (2011).
10. P. Lankaster, *Theory of matrices* (Academic Press, New York – London, 1969).
11. L. D. Landau and E. M. Lifshitz, *Electrodinamics of Continuous Media*, Course of Theoretical Physics (Pergamon Press, New York, 1960), 2nd ed. Ch. 9.
12. A. K. Popov, I. S. Nefedov, and S. A. Myslivets, *arXiv*:1602.02497.
13. L. V. Alekseyev and E. Narimanov, Opt. Express **14**, 11184 (2006).

REFERENCES

1. W. Cai and V. Shalaev, *Optical metamaterials, fundamentals and applications* (Springer-Verlag, New York, 2010), 1st ed.

2. A. K. Popov and V. M. Shalaev, "Negative-index metamaterials: second-harmonic generation, manley rowe relations and parametric amplification," Appl. Phys. B: Lasers and Optics **84**, 131–137 (2006).

3. I. V. Shadrivov, A. A. Zharov, and Y. S. Kivshar, "Second-harmonic generation in nonlinear left-handed metamaterials," J. Opt. Soc. Am. B **23**, 529–534 (2006).

4. M. Lapine, I. V. Shadrivov, and Y. S. Kivshar, "*Colloquium*: Nonlinear metamaterials," Review of Modern Physics **86**, 1093–1123 (2014).

5. A. K. Popov, M. I. Shalaev, S. A. Myslivets, V. V. Slabko, and I. S. Nefedov, "Enhancing coherent nonlinear-optical processes in nonmagnetic backward-wave materials," Appl. Phys. A **109**, 835–840 (2012).

6. A. Poddubny, I. Iorsh, P. Belov, and Yu. Kivshar, "Hyperbolic metamaterials," Nat. Phot. **7**, 948–957 (2013).

7. I. V. Lindell, S. A. Tretyakov, K. I. Nikoskinen, and S. Ilvonen, "Bw media – media with negative parameters, capable of supporting backward waves," Microwave and Optical Technology Letters **31**, 129–133 (2001).

8. I. Nefedov and S. Tretyakov, "Effective medium model for two-dimensional periodic arrays of carbon nanotubes," Photonics and Nanostructures – Fundamentals and Applications **9**, 374 – 380 (2011).

9. I. Nefedov and S. Tretyakov, "Ultrabroadband electromagnetically indefinite medium formed by aligned carbon nanotubes," Phys. Rev. B **84**, 113410 (2011).

10. P. Lankaster, *Theory of matrices* (Academic Press, New York – London, 1969).

11. L. D. Landau and E. M. Lifshitz, *Electrodinamics of Continuous Media*, Course of Theoretical Physics (Pergamon Press, New York, 1960), 2nd ed. Ch. 9.

12. A. K. Popov, I. S. Nefedov, and S. A. Myslivets, "Phase Matched Backward-wave Second Harmonic Generation in a Hyperbolic Carbon Nanoforest," *arXiv*:1602.02497 .

13. L. V. Alekseyev and E. Narimanov, "Slow light and 3D imaging with non-magnetic negative index systems," Opt. Express **14**, 11184-11193 (2006).